

Bootstrap 3D Reconstructed Scenes from 3D Gaussian Splatting

Yifei Gao^{1*} Jie Ou³ Lei Wang^{2†} Jun Cheng²

¹University of Electronic Science and Technology of China,

²Shenzhen Institutes of Advanced Technology, Chinese Academy of Sciences,

³Sichuan Yuanzhigu Technology Co., Ltd



Figure 1. Our bootstrapping technique effectively compensates for the artifacts observed in 3D-GS by generating pseudo-details. This approach involves introducing synthesized visual elements that, while not part of the original dataset, are designed to integrate seamlessly with the genuine features of the scene.

Abstract

Recent developments in neural rendering techniques have greatly enhanced the rendering of photo-realistic 3D scenes across both academic and commercial fields. The latest method, known as 3D Gaussian Splatting (3D-GS), has set new benchmarks for rendering quality and speed. Nevertheless, the limitations of 3D-GS become pronounced in synthesizing new viewpoints, especially for views that greatly deviate from those seen during training. Additionally, issues such as dilation and aliasing arise when zooming in or out. These challenges can all be traced back to a single underlying issue: insufficient sampling. In our paper, we present a bootstrapping method that significantly addresses this problem. This approach employs a diffusion model to enhance the rendering of novel views using trained 3D-GS, thereby streamlining the training process. Our results indicate that bootstrapping effectively reduces artifacts, as well as clear enhancements on the evaluation metrics. Furthermore, we show that our method is versatile and can be easily integrated, allowing various 3D reconstruction projects to benefit from our approach.

1. Introduction

The quest for photo-realistic and real-time 3D scene rendering holds significant interest in both scholarly research and the industrial sector, finding use in virtual reality [80],

media production [45], and the visualization of extensive scenes [46, 47, 51]. Traditional methods such as volumetric approaches and neural radiance fields (NeRF) leverage learning-based models [4, 33, 38] to achieve renderings that are continuous and detail-rich. However, this advanced quality comes at the expense of extensive stochastic sampling, which slows down the process and may introduce noise. On the other hand, meshes and point-based [12, 13, 43, 44] representations offer speed advantages due to their compatibility with rasterization techniques optimized for contemporary GPUs. Yet, these approaches often result in renderings of lower quality, marred by discontinuities and blurriness.

Lately, 3D Gaussian Splatting (3D-GS) [1] has emerged as a cutting-edge method in rendering, demonstrating unparalleled quality and efficiency. 3D-GS captures 3D scenes using points modeled as 3D Gaussians, incorporating view-dependent colors through Spherical Harmonics. This approach achieves both high-quality visualization and rapid rasterization simultaneously.

Despite its significant advancements, this method encounters a critical limitation inherent to its foundational principle: 3D-GS seeks to replicate scenes using 3D Gaussians but lacks the ability to accurately render entirely unseen views or views that greatly diverge from the primary training perspectives, often resulting in a jumbled mess, as shown in Fig 2. Additionally, recent studies [31] have

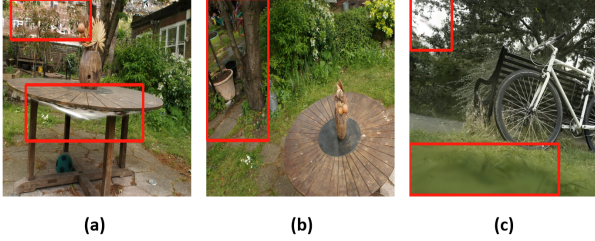


Figure 2. **3D-GS Artifacts.** The original 3D-GS [1] exhibits significant artifacts during certain novel-view renderings. Specifically, (a) presents the unseen view (under the table); (b) the undersampled view; and (c) the view significantly divergent from training cameras.

highlighted that adjusting the camera’s zoom during rendering can lead to noticeable flaws, including dilation or high-frequency artifacts, in the rendered scenes.

In this paper, we present a bootstrapping method that uses already-trained 3D Gaussians to render the wield views. Diffusion models are utilized to refine these rendered views, which are then incorporated back into the training. Instead of addressing the inherent flaws of the 3D-GS through limitations or regularizations on 3D Gaussians model as contemporary works do [31], we aim to rectify this issue by focusing on improving the sampling process. By thoroughly leveraging the principle of the diffusion model, we proved the effectiveness of our method. Furthermore, we showcase the advancement of our method and its broad application across various implementations.

Our main contributions are as follows: 1) Validation of our bootstrapping technique’s effectiveness; 2) Comprehensive advancements over prior state-of-the-art efforts and the original 3D-GS; 3) Demonstrating the plug-and-play capability of our method and its extensive applicability.

2. Related work

2.1. Diffusion Models

Introduction of Diffusion Model. Diffusion models [6] are latent variable models of the form $p_\theta(\mathbf{x}_0) := \int p_\theta(\mathbf{x}_{0:T}) d\mathbf{x}_{1:T}$, where $\mathbf{x}_1, \dots, \mathbf{x}_T$ are latents of the same dimensionality as the data $\mathbf{x}_0 \sim q(\mathbf{x}_0)$. The *forward process*, also known as the *diffusion process*, is established as a Markov chain that incrementally introduces Gaussian noise into the data, guided by a predetermined variance schedule. Conversely, the *reverse process* refers to the joint distribution $p_\theta(\mathbf{x}_{0:T})$ and it is also defined as a Markov chain with learned Gaussian transitions starting at

$$p(\mathbf{x}_T) = \mathcal{N}(\mathbf{x}_T; \mathbf{0}, \mathbf{I}):$$

$$p_\theta(\mathbf{x}_{0:T}) := p(\mathbf{x}_T) \prod_{t=1}^T p_\theta(\mathbf{x}_{t-1}|\mathbf{x}_t), \quad (1)$$

$$p_\theta(\mathbf{x}_{t-1}|\mathbf{x}_t) := \mathcal{N}(\mathbf{x}_{t-1}; \boldsymbol{\mu}_\theta(\mathbf{x}_t, t), \boldsymbol{\Sigma}_\theta(\mathbf{x}_t, t)) \quad (2)$$

In this process, the original distribution at time step $\mathbf{0}$ is gradually recovered from time step \mathbf{T} . And training is performed by optimizing the usual variational bound on negative log likelihood. If all the conditionals are modeled as Gaussians with trainable mean functions and fixed variances, the training objective can be simplified to:

$$L_{\text{simple}}(\theta) := \mathbb{E}_{t, \mathbf{x}_0, \epsilon} \left[\left\| \epsilon - \epsilon_\theta(\sqrt{\bar{\alpha}_t} \mathbf{x}_0 + \sqrt{1 - \bar{\alpha}_t} \epsilon, t) \right\|^2 \right] \quad (3)$$

where ϵ_θ is a learned noise prediction function, $\bar{\alpha}_t$ the schedule factor, and ϵ a random normal. For more details, please see in [27–29]

Image-to-Image Generation. Image-to-image generation represents a practical application of diffusion models. This paper specifically addresses a unique form of generation wherein an input image is regenerated by the diffusion model, utilizing a defined broken strength s_r to facilitate controlled generation. In this approach, only a partial reverse process is engaged. The magnitude of s_r directly influences the degree of deviation in the output image from the original, with larger s_r values resulting in greater alterations. For example, if the $s_r = 0.1$ and the total time step $T = 1000$, then during the reverse diffusion process, diffusion is directly applied at the time step $T \times s_r = 100$. In other words, only the last 100 time steps of the reverse diffusion process are executed to conduct moderate regeneration.

2.2. 3D-GS

3D-GS [1] models the scene using a collection of anisotropic 3D Gaussians, which embody the differential attributes of a volumetric representation. This approach allows for efficient rendering through tile-based rasterization, combining the detailed spatial variation inherent in volumetric data with the computational efficiency of traditional rendering techniques.

Beginning with a collection of points derived from Structure-from-Motion (SfM), each point is assigned as the position (mean) μ of a 3D Gaussian:

$$G(x) = e^{-\frac{1}{2}(x-\mu)^T \Sigma^{-1}(x-\mu)}, \quad (4)$$

In this context, x represents any arbitrary position within the 3D scene, and Σ signifies the covariance matrix of the 3D Gaussian. The covariance matrix Σ is constructed utilizing

a scaling matrix S and a rotation matrix R , ensuring that it remains positive semi-definite:

$$\Sigma = RSS^T R^T, \quad (5)$$

Besides modeling color c through Spherical harmonics, each 3D Gaussian is linked with an opacity α . This opacity is factored into $G(x)$ during the blending procedure, allowing for the nuanced integration of color and transparency attributes within the rendered scene, enhancing the realism and depth of the visual output.

Unlike traditional volumetric representations that rely on resource-intensive ray-marching techniques for rendering, 3D-GS achieves efficient scene rendering through tile-based rasterization. This process involves initially converting the 3D Gaussians $G(x)$ into 2D Gaussians $G'(x)$ on the image plane as a result of the projection process described in [82]. Subsequently, a specially designed tile-based rasterizer sorts these 2D Gaussians and applies α -blending:

$$C(x') = \sum_{i \in N} c_i \sigma_i \prod_{j=1}^{i-1} (1 - \sigma_j), \quad \sigma_i = \alpha_i G'_i(x'), \quad (6)$$

where x' is the queried pixel position and N denotes the number of sorted 2D Gaussians associated with the queried pixel. By utilizing a differentiable rasterizer, all attributes of the 3D Gaussians become learnable and can be directly optimized in an end-to-end manner through the process of training view reconstruction.

3. Methods

3.1. Bootstrapping by Diffusion Model

For a novel-view image synthesized by the trained 3D-GS model, its fidelity to the ground truth image may be compromised due to the presence of unseen parts not included in the training dataset. In instances where this novel-view image is considered a "partially degenerated" version of the ground truth, a diffusion model can be utilized to perform image-to-image integration on the synthesized image to approximate the ground truth image, as described in Sec. 2.1. Given novel-view RGB image $\mathbf{I} \in \mathbb{R}^{w \times h \times 3}$, there exists a differential $\delta_i \in \mathbb{R}^{w \times h \times 3}$ generated by diffusion models that facilitates this image integration:

$$\mathbf{I}' = \delta_i + \mathbf{I}, \quad (7)$$

where w and h are the width and height of \mathbf{I} , and \mathbf{I}' is the regenerated image. Then using the diffusion process, we can reformulate the δ_i as a collection of diffusion noise generated by the noise predictor:

$$\delta_i = \sum_{t \in T_{sr}} \epsilon_\theta(\sqrt{\bar{\alpha}_t} \mathbf{x}_t(\mathbf{I}, \epsilon) + \sqrt{1 - \bar{\alpha}_t} \epsilon, t), \quad (8)$$

Here, \mathbf{x}_t is a function of \mathbf{I} and ϵ (we write in this form just for simplicity and better comprehension, for detail please see [27, 28]).

Under this framework, the degree to which the generated image variance δ_i aligns with the ground truth image variance δ'_i directly correlates to the improvement in our results. However, achieving the ideal situation in practice is very difficult. This is not only because (1) the currently available open-source diffusion models cannot perform well in generating partial images in all scenarios, but also because (2) many scenarios themselves are complex and unique. Moreover, (3) the very process of bootstrapping introduces a level of uncertainty. Ideally, the constructed 3D scene would appear consistent across all perspectives. However, the variability introduced by the diffusion model makes it challenging to guarantee that scenes regenerated by the diffusion model from one new viewpoint will seamlessly align with those from another. Additionally, (4) not all parts of the synthesized novel-view images should be regenerated, if we apply the diffusion process to the whole image, some already well-trained parts will be distorted to some extent. Therefore, based on these problems, we have explored a more universally usable and more stable method.

3.2. Bootstrapping Design

Bootstrapping Issues. Regarding the issue of overall scene consistency, it requires the start of bootstrapping from a relatively complete stage on reconstructed 3D scenes with small diffusion broken strength. In the context of image regeneration using diffusion models, if the surrounding context is homogeneous and exhibits similarity, it can be inferred that the regenerated content within our setting demonstrates minimal variation. This observation arises because the diffusion process is applied only during several final time steps. By definition, the scale factor $\sqrt{1 - \bar{\alpha}_t}$, which governs the magnitude of noise added, approaches zero as the time schedule t approaches zero, as delineated in [6, 27]. We constrain the range of the time schedule to ensure that the value of $\sqrt{1 - \bar{\alpha}_t}$ remains small. This constraint guarantees that the value of δ_i is also maintained at a minimal level.

We bootstrap every training image with its novel-view variants. To get a novel-view image \mathbf{I}_t^n from a training image \mathbf{I}_t , we first construct a set of new camera parameters for rendering. In the COLMAP [19, 20] form, we solely slightly change a training camera's *qvec* and *tvec* to obtain new view cameras, as detailed further in Sec. 4.1. Then we regenerate \mathbf{I}_t^n by diffusion model and get \mathbf{I}_t^b

Bootstrapping Loss. The regenerated image \mathbf{I}_t^b can be categorized into two parts: one that contains a faithful representation of the scene but changed with alterations, and another that exhibits an incomplete or inaccurate depiction

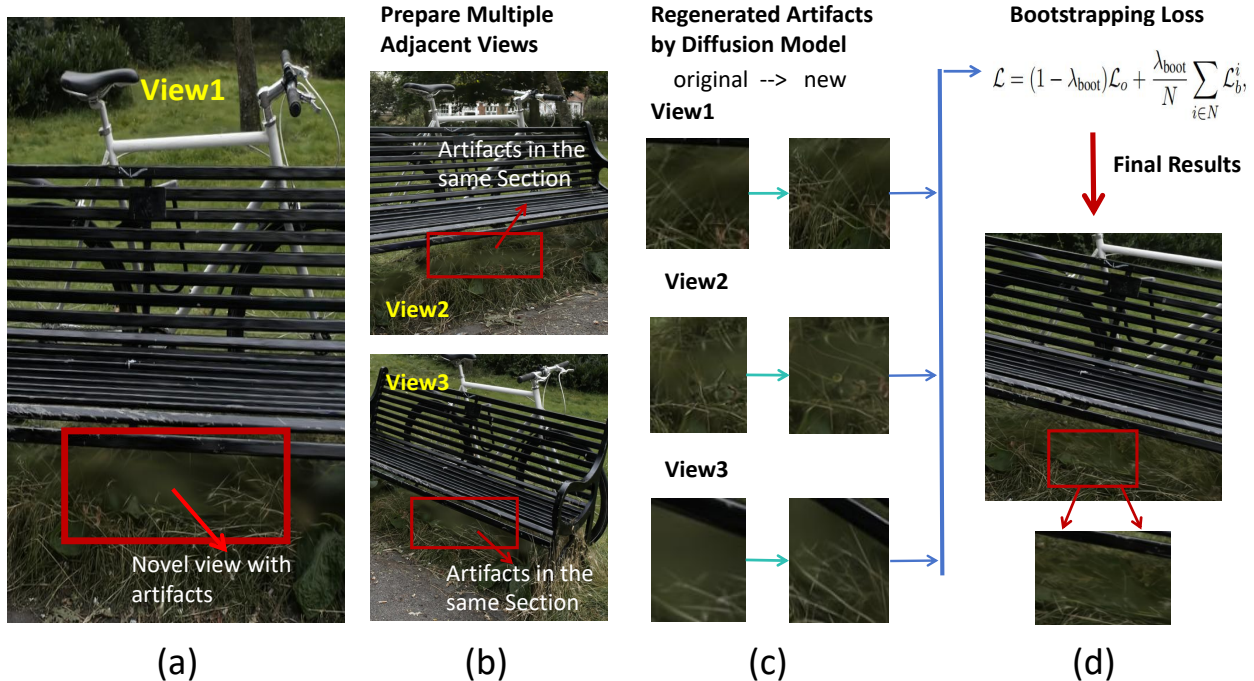


Figure 3. **Training Pipeline.** For novel-view rendering with artifacts (a), we initially prepare multiple adjacent novel-view renderings, ensuring the inclusion of the imperfect segment in each view (b). Subsequently, we regenerate all the views utilizing the diffusion model (c). Finally, through the application of our tailored training strategies, the final result demonstrates significant enhancement in the quality of the imperfect part (d).

of the scene, having been modified by the diffusion model. By managing the ratio of the loss associated with the original training component and that of the bootstrapping component, we can achieve a globally stable training process for the 3D-GS model and attain superior results.

We set our bootstrapping loss term \mathcal{L}_b as \mathcal{L}_1 loss of the novel-view rendered image \mathbf{I}_t^n with the regenerated image \mathbf{I}_t^d , where $\mathcal{L}_b = \|\mathbf{I}_t^n - \mathbf{I}_t^d\|$. During training, if bootstrapping is used, then for every training camera, we use a hybrid loss with a small scaling factor λ_{boot} that

$$\mathcal{L} = (1 - \lambda_{boot})\mathcal{L}_o + \frac{\lambda_{boot}}{N} \sum_{i \in N} \mathcal{L}_b^i, \quad (9)$$

where \mathcal{L}_o is the original 3D-GS training loss with ground-truth image [1], $\sum_{i \in N} \mathcal{L}_b^i$ is the cumulative bootstrapping loss across all bootstrapping views used in training this camera, and N is the total variant number. The bootstrapping views employed are derived from all novel-view camera variants, which are based on the training camera and its surrounding cameras. For example, if the training camera has both sides of surrounding cameras and we bootstrap each camera with 2 of its variants, then the N is 6. This design choice is motivated by the common characteristic of most 3D reconstruction datasets [83–85], where cameras positioned in close proximity typically capture adjacent

scenes.

When the λ_{boot} is sufficiently small, such as 0.05, it becomes evident that the bootstrapping loss term will have minimal effects in the first scenario, in which well-trained parts are subject to alteration. For those parts or viewing angles that are underrepresented in the training dataset, where renderings appear visibly disordered or lack detail, the bootstrapping term can effectively facilitate modifications that remain consistent across multiple viewpoints. In our methodology, the bootstrapping scenarios consistently incorporate some of the same degenerated parts within our loss term configuration. Consequently, these parts are processed repeatedly from multiple angles, and the values are averaged over these areas to ensure uniformity and improve the overall quality of the synthesized views.

3.3. Methodological Analysis

In this section, our discussion will focus exclusively on the imperfect parts of the regenerated image (as described in the second scenario above), since the well-trained components of the model are relatively insensitive to our bootstrapping technique and can be easily rectified.

Emphasis on Cloning Direction. In the optimization process of 3D-GS, starting from a sparse set of COLMAP

points, 3D-GS model will end up with millions of small and dense 3D Gaussians. Our bootstrapping technique particularly emphasizes the cloning function in training. During the densification process, where points are either split or cloned, the surrounding points of these imperfect sections are initially flattened to compensate for the inconsistencies in the regenerated novel-view renderings. After several iterations’ accumulation, big points are split into smaller ones, and small points are cloned along the gradient direction. In practical terms, these large points can be considered as coarse aggregations of smaller Gaussian points, where the renderings of these formations appear blurred. Over time, as the 3D-GS model progresses and refines, these big points gradually diminish and are refined into finer details. As such, they typically cease to exist in the final stages of the model’s training.

In conclusion, while large points may be noticeable in earlier phases, their overall impact on the final output of the model is minimal. Therefore, our primary focus should shift towards the cloning aspect. Specifically, we emphasize the gradient direction within the cloning procedure to ensure that finer details are accurately replicated and preserved, enhancing the overall fidelity and granularity of the scene.

Theoretical Analysis The training process with bootstrapping tends to be unstable, as the regenerated renderings vary from each other even within the same scene section. We parameterize a Gaussian point with its position $\mu \in \mathbb{R}^3$, opacity $\alpha \in \mathbb{R}$, covariance-related quaternion $q \in \mathbb{R}^4$, scaling $s \in \mathbb{R}^3$, and color $c \in \mathbb{R}^3$. Each of these parameters is optimized simultaneously yet separately, allowing us to treat their gradients as independent. For the purpose of this analysis, we will consider a generalized situation.

The gradients generated by the bootstrapping term originate from the regeneration capabilities of the diffusion model, which prompts our initial focus on the diffusion process. Ideally, a well-trained diffusion model, as defined by nonequilibrium-thermodynamics diffusion models in [6], can reconstruct the original image from random noise through an infinite sequence of reverse diffusion sampling. Achieving this ideal scenario necessitates two conditions: (1) the model’s inherent capability to accurately simulate complex scenarios, and (2) an unlimited number of reverse time steps. In our experimental framework, we conduct only incomplete reverse diffusion processes with extremely limited time steps. Therefore, we can assume that our model adequately fulfills the capability requirements. Following condition (2), after infinite reverse sampling, all generated content should be identical, given the same initial states. If variations still occur after regeneration within the same defective segment, these can be attributed to the limited time step schedule. To address this issue, we can manually inte-

grate reverse sampling into our process.

On a Gaussian point, for a gradient $\partial g_b \in \mathbb{R}^d$ generated through the bootstrapping image and another gradient $\partial g \in \mathbb{R}^d$ derived from the ground-truth image, where d is the dimension. it is reasonable to consider ∂g_b as a degenerated version of ∂g influenced by insufficient sampling:

$$\partial g = \delta_b + \partial g_b, \quad (10)$$

where δ_b is the gradient difference. By the formulation specified in our loss term Eq.9, a Gaussian point typically encounters multiple bootstrapping gradients within a single training camera session. The bootstrapping differential δ_i in Eq 8, is conceptualized as a collection of noise, and our loss term is designed to facilitate the aggregation of these diverse noise collections. We can reformulate the bootstrapping loss $\sum_{i \in N} \mathcal{L}_b^i$ part as

$$\sum_{i \in N} \mathcal{L}_b^i \propto \sum_{i \in N} \sum_{t \in T_{s,r}} \epsilon_\theta(\sqrt{\bar{\alpha}_t} \mathbf{x}_t(\mathbf{I}_b^i, \epsilon) + \sqrt{1 - \bar{\alpha}_t} \epsilon, t), \quad (11)$$

where \mathbf{I}_b^i is the i th bootstrapping image. Given our focus on the imperfect segments, and considering that each segment’s surrounding context is similar and homogeneous as described in Sec 3.2, we can approximate each \mathbf{I}_b^i within that segment as identical. Then, for each defective segment, we can rewrite Eq.11:

$$\sum_{i \in N} \mathcal{L}_b^i \propto N \sum_{t \in T_{s,r}} \epsilon_\theta(\sqrt{\bar{\alpha}_t} \mathbf{x}_t(\mathbf{I}_b, \epsilon) + \sqrt{1 - \bar{\alpha}_t} \epsilon, t), \quad (12)$$

As such, we integrate the defective segments with N times repeated reverse sampling of bootstrapping. This process inherently compensates for the issue of insufficient sampling by aggregation, thereby enhancing content generation to be more consistent.

Practical Cloning Design Experimentally, we hypothesize that the diffusion model typically generates images that are contextually aligned but vary in detail. However, even with multiple times of reverse sampling, some normalized variances remain significantly large when compared to ground-truth images. For simplification, we project the d -dimensional gradient onto a 2D xy-plane, with the positive y-axis directed towards ∂g_b and other directions indicating deviations. By setting an appropriate threshold for the gradient accumulation magnitude during cloning, we can achieve a more stable optimization outcome, as shown in Fig 4. After several rounds of splitting, points will be small enough and only a small amount of gradients will occur at those points (even if not, the λ_{boot} is small enough). For further cloning, only these gradients oriented precisely in one direction with small deviations have the potential to exceed that threshold. Then we get a relatively faithful bootstrapping cloning point that constitutes the detail in that scene.

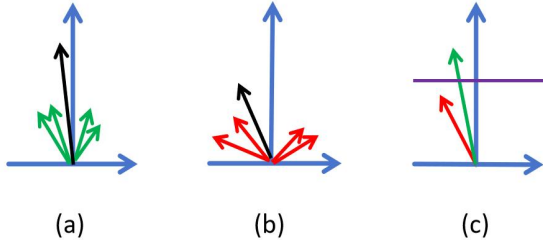


Figure 4. **2D Gradient Accumulation.** Given four gradient directions to compose accumulation, **black** vector is their accumulation. (a) Vectors generally towards the y direction with small deviations; (b) Vectors demonstrate larger deviations. (c) By setting a **threshold** on their accumulations, we can filter out gradients accumulation with large deviations.

4. Experiments

4.1. Experimental Setup

Dataset and Metrics. Our experiments are conducted on publicly available mainstream 3D reconstruction datasets, following the 3D-GS [1]. They include seven scenes from Mip-NeRF360 [83], two scenes from Tanks&Temples [84], and two scenes from DeepBlending [85]. The evaluation metrics are PSNR, SSIM [52], and LPIPS [53]), together with training time. The efficiency issues (e.g. rendering speed and storage size) are not primary concerns in our study, given that our technique centers on bootstrapping. The diffusion process and the bootstrapping loss described in Eq. 9, inherently require additional time to execute. In the main paper, we present averaged metrics for all scenes from each dataset, while detailed quantitative results for individual scenes are provided in the supplementary materials.

Baseline and Implementation. Our baselines are selected based on original 3D-GS [1], Mip-NeRF360 [83], iNGP [10] and Plenoxels [9], combining with recently advanced Scaffold-GS [35]. Following the original 3D-GS, we also report our 7k and 30k results. In our experiments, we keep the same Gaussian model and dataset configurations as in [1]. For our bootstrapping part, we utilize the **Stable Diffusion (SD) 2v.1** model [30] and its finetuned models as our initial diffusion models. We conduct 4 stages of experiments, where when and how bootstrapping is applied are different.

In the initial stage of our experiment, we perform bootstrapping at specific intervals, dedicating 1000 iterations to each bootstrapping span. During each of these 1000-iteration intervals, we set the λ_{boot} to 0.15 for the first 500 iterations and reduce it to 0.05 for the remaining 500 iter-

ations. In configuring the diffusion model, we employ a progressively decreasing image broken strength s_r , ranging from 0.05 to 0.01, across 100 time steps of DDIM [28] sampling. For various datasets, we implemented different strategies for creating novel-view cameras (**Random** or **Consecutive**). The bootstrapping regenerated images are executed using the original **SD2.1v** model. For the second stage experiment, the **SD2.1v** model is finetuned separately on each training dataset while leaving other configurations unchanged. The decision to finetune the **SD2.1v** model was based on empirical findings from our initial stage experiments, not a mere whim. After completing these experiments, we observed significant fluctuations in our results: while some scenes showed clear progress in metrics, others exhibited noticeable degradation, which is further discussed in Sec. 4.2. We also provide a detailed explanation of this configuration and the finetuning strategy of **SD2.1v** model in our supplementary material.

After fine-tuning models for each scene, we aim to further unlock the potential of bootstrapping. Therefore, in our third stage experiments, we adjust the diffusion broken strength s_r from 0.15 to 0.01, with all creations of bootstrapping images set to **Random** for every scene. While experiments across the initial three stages have demonstrated considerable improvements over the original 3D-GS, challenges persist in rendering specific views. To address this, in our fourth stage experiments, we additionally employ an upscale diffusion model for our bootstrapping regeneration, which can be found in our supplementary material.

4.2. Results Analysis

The effectiveness of our bootstrapping approach has been demonstrated across various scenes, particularly in challenging environments characterized by texture-less surfaces and insufficient observations. Additionally, the method shows its adaptability when altering cameras for novel-view rendering, highlighting its proficiency in capturing homogeneous nuances as shown in Fig 5.

Metrics Comparisons. In assessing the quality of our approach, we compared with 3D-GS [1], Mip-NeRF360 [83], iNGP [10], Plenoxels [9] and Scaffold-GS [35] on real-world datasets. Qualitative results are presented in Tab. 1. The quality metrics for Mip-NeRF360, iNGP and Plenoxels align with those reported in the 3D-GS study. It’s clear that our bootstrapping technique can indeed largely leverage the 3D-GS’s potential, as we do not change the original 3D-GS model and only add additional training cameras through our technique. The improvement of the quality metrics can be traced back to 7k iterations after applying only one interval’s bootstrapping compared with the original 3D-GS (The original 7k metrics can be seen in [1]). Even simply applying the **SD2.1v** model in our first stage experiments,



Figure 5. **Qualitative comparison of our two stage results and 3D-GS [1] across diverse datasets [83].** Patches that highlight the visual differences are emphasized with **square** for clearer visibility. Our approach constantly outperforms 3D-GS on these scenes, with evident advantages in challenging scenarios.

Table 1. **Quantitative comparison to previous methods on 3 datasets.** Competing metrics are sourced directly from the respective papers. For 3D-GS and Scaffold-GS, the results are on its 30k iterations. Our best results may not be achieved by the 30k iterations because of the bootstrapping, so we only exhibit our best results as *best*. We denote *v1* as our first-stage experiments and *v2* as the second-stage experiments respectively.

Dataset Method Metrics	Mip-NeRF360			Tanks&Temples			Deep Blending		
	PSNR \uparrow	SSIM \uparrow	LPIPS \downarrow	PSNR \uparrow	SSIM \uparrow	LPIPS \downarrow	PSNR \uparrow	SSIM \uparrow	LPIPS \downarrow
3D-GS [1]	28.69	0.870	0.182	23.14	0.841	0.183	29.41	0.903	0.243
Mip-NeRF360 [83]	29.23	0.844	0.207	22.22	0.759	0.257	29.40	0.901	0.245
iNPG [10]	26.43	0.725	0.339	21.72	0.723	0.330	23.62	0.797	0.423
Plenoxels [9]	23.62	0.670	0.443	21.08	0.719	0.379	23.06	0.795	0.510
Scaffold-GS [35]	28.84	0.848	0.220	23.96	0.853	0.177	30.21	0.906	0.254
Ours-v1-7k	27.363	0.833	0.239	21.750	0.784	0.261	28.562	0.885	0.302
Ours-v2-7k	27.623	0.837	0.259	22.102	0.788	0.259	29.346	0.891	0.297
Ours-v1-best	29.057	0.872	0.182	23.709	0.849	0.176	29.960	0.905	0.242
Ours-v2-best	29.668	0.885	0.179	24.398	0.859	0.171	31.565	0.917	0.231

we can see significant progress compared with the original 3D-GS which is even compatible with recently advanced Scaffold-GS. Moreover, after fine-tuning the **SD2.1v** model for each scene, we achieved the best results across all datasets and metrics compared to existing methods, surpassing even Mip-NeRF 360 in performance on their own dataset. Given that the overall performance metrics of our third-stage experiments are similar to those observed in our second-stage experiments, we have chosen to provide detailed reporting of the metrics specific to each scene from

our third-stage experiments in our supplementary material.

Alleviation of Novel-view Artifacts Our improvement is evident not only in the metrics. As previously mentioned, we also addressed issues such as artifacts that occur when changing the camera zoom or rendering views that significantly diverge from the training sets [31] to some extent. Bootstrapping mitigates artifacts observed in the original 3D-GS by generating pseudo-details as shown in Fig 6. By the conclusion of our third-stage experiments, we ob-

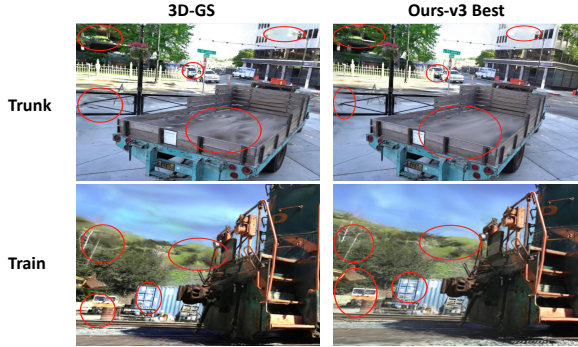


Figure 6. **Comparison on novel-view scenes.** We showcase the rendering outcomes at views far divergent from training sets. In these unseen views, 3D-GS tends to generate distorted details to better align with the training sets, whereas our approach compensates for this distortion by generating pseudo-details.



Figure 7. **Comparison on novel-view scenes.** While the original 3D-GS tends to render unseen views as blurry, our fourth-stage experiments demonstrate the capability to generate sharp details based on the surrounding context.

served that artifacts occurring in specific views could indeed be alleviated while maintaining strong performance metrics. However, there remains considerable potential for further improvement. Given that our technique has already achieved superior results, our fourth-stage experiments will primarily focus on further alleviating these artifacts. Details of our fourth-stage experiments are illustrated in our appendix. From Fig 1 and 7, it is evident that our fourth-stage results show clear improvements over both the original 3D-GS and our third-stage outcomes. Distortions observed in the undersampled view and the jumbled mass under the table have been substantially modified. After completing our fourth-stage experiments on the Mip-NeRF 360 datasets [83], we observed that the application of the upscale diffusion model is particularly effective in open scenes that encompass many unseen views (maybe because we do not finetune it). For most indoor scenes, the introduction of significant noise through the upscale diffusion model tends

Table 2. **Time comparison.** We report our 30k training time consumption. And it should be noted that in our second-stage experiments, the sole alteration involves the diffusion model. Consequently, the time consumption in the first stage remains identical to that of the second stage.

Dataset	Mip-NeRF360	Tanks&Temples	Deep Blending
3D-GS	41min	26min	36min
Ours-v1	96min	64min	81min
Ours-v3	117min	84min	104min

to negatively impact the performance metrics substantially, as detailed in our appendix.

Time Consumption Thanks to the 3D-GS’s fast training and adaptation to reconstruction, our technique can have an opportunity to make use of its potential. The central increase in time consumption for our technique stems from the diffusion process introduced by bootstrapping. On the other hand, the multi-view rasterization, as required in Eq. 9, has minimal impact on the overall time required. Our time consumption comparisons are exhibited in Tab 2. Generally, the increase in diffusion time steps, which is related to the broken strength s_r , significantly contributes to additional training time.

Feature Analysis. We also made comparisons of rendering details across our four-stage experiments. During the initial two stages, if we evaluate solely based on the generation quality without considering the metrics, there appears to be minor variance in their quality. After fine-tuning for each specific scene, we observed significant progress in context-specific details. For instance, in Fig 5 **Room**, consider the camera object (the middle one in zoomed-in details) above the door. In our first-stage experiment, the camera was only represented in a basic form resembling a camera. However, in our second-stage experiment, the camera displayed curves similar to those in the ground truth. Then in our third-stage experiments, although the details were altered and refined due to increased DDIM sampling steps, as seen in Fig 6, these alterations were unable to fully compensate for the substantial deficiencies present in the scene. Furthermore, these generated details tend to occur at low frequencies, which is closely related to our loss term. Since our approach emphasizes enhancing details that harmonize rather than conflict with each other, the high-frequency details generated by the diffusion model tend to exhibit variability. Ultimately, while our fourth-stage experiments were capable of significantly modifying the unseen content, these changes did not necessarily translate into improved metrics. This is because the fine-grained details generated might not always accurately reflect the actual ground truth details.

Table 3. **Ablation studies.** In our setup, the broken strength s_r decreases in conjunction with the integration of the 3D-GS model. Additionally, the values of λ_{boot} are individually tailored, as detailed in Sec. 4.1. Our consecutive bootstrapping results for finetuned model have variations. with **L** the lowest one and **H** the highest one.

Scene	DRJHONSON			PLAYROOM		
	PSNR	SSIM	LPIPS	PSNR	SSIM	LPIPS
s_r Range: [0.25,0.05]	28.815	0.894	0.248	30.096	0.903	0.245
λ_{boot} : [0.05, 0.05]	28.913	0.899	0.244	30.192	0.907	0.243
λ_{boot} : [0.25, 0.05]	27.675	0.893	0.252	29.394	0.892	0.249
λ_{boot} : [0.25, 0.15]	27.527	0.886	0.259	29.161	0.884	0.245
No Text Prompt	29.056	0.901	0.244	30.284	0.908	0.243
Consecutive	26.818	0.872	0.271	28.534	0.869	0.255
Consecutive(Finetuned)- L	28.214	0.895	0.247	29.521	0.898	0.247
Consecutive(Finetuned)- H	31.124	0.916	0.230	32.216	0.921	0.231
BASIC	29.063	0.901	0.244	30.296	0.909	0.243

4.3. Ablation Studies

Our ablation studies are mainly tested on the configuration of the diffusion model, specifically on how we regenerate the bootstrapping images. We have evaluated various hyperparameters of the diffusion model, with some outcomes outlined in Tab 3. Our results indicate that only the broken strength s_r and the loss weight λ_{boot} are significant. Common hyperparameters that typically influence the outcomes in the traditional text-to-image generation, such as text prompt, text prompt scale, and eta as described in [30], have minimal impact in our experimental setup. As detailed in Sec. 4.1, we apply our bootstrapping technique only during specific intervals. We have also conducted consecutive bootstrapping with every bootstrapping interval after the 6,000th iteration but discovered that this approach led to instability. Continuous bootstrapping, when overused, tends to generate scenes that are completely out of context. Even when finetuning the diffusion model specifically for each scene, its instability remains a significant issue. The highest results achieved through consecutive bootstrapping in the second-stage setting occasionally surpass those of our best records. However, achieving these superior outcomes is quite challenging, and the training time required is approximately 2.5 times compared to the original second-stage experiments. This significant increase in time and effort highlights the inefficiency of consecutive bootstrapping despite its potential for achieving slightly better performance metrics. Notice that our other basic ablation studies are all tested on our first-stage experiment’s configuration.

4.4. Discussions and Limitations

Through our experiments, we identified that the main challenge in implementing our approach is the time consumption. Achieving desirable results often necessitates extended periods in the diffusion process across different experimental stages. Specifically, while we can achieve excellent outcomes in our second-stage experiments, training the

3D-GS model requires hours. In addition, we extended our approach to incorporate multi-scale 3D datasets [51]. While this extension yielded promising results in comparison to the original 3D-GS, it also revealed notable limitations, as outlined in our appendix. However, given that our technique is designed as a plug-and-play solution, we anticipate it will evolve and improve as advancements are made in this field. Further details are discussed in the supplementary material.

5. Conclusion

In this study, we introduce the **bootstrapping** technique, which employs a diffusion model to fill in the missing parts of the training dataset scenario. The essence of our technique is its precise targeting and effective solutions to address the issue of missing information in reconstruction efforts. As a plug-and-play method, we demonstrate that after implementing bootstrapping, the original 3D-GS can achieve state-of-the-art (SOTA) results, even when compared with its more recent counterparts. Additionally, our technique not only enhances the metrics but also refines the artifacts in 3D-GS that are not detectable through metrics alone. Moreover, our technology tackles a wide range of issues related to deficient sampling in 3D reconstruction, extending beyond just 3D-GS applications. Therefore, our approach holds substantial potential for broader applications.

References

- [1] B. Kerbl, G. Kopanas, T. Leimkühler, and G. Drettakis, “3d gaussian splatting for real-time radiance field rendering,” *ACM Transactions on Graphics*, vol. 42, no. 4, July 2023. [Online]. Available: <https://repo-sam.inria.fr/fungraph/3d-gaussian-splatting/> 1, 2, 4, 6, 7, 3
- [2] T. Takikawa, J. Litalien, K. Yin, K. Kreis, C. Loop, D. Nowrouzezahrai, A. Jacobson, M. McGuire, and S. Fidler, “Neural geometric level of detail: Real-time rendering with implicit 3d shapes,” in *Proceedings of the IEEE/CVF Conference on Computer Vision and Pattern Recognition*, 2021, pp. 11 358–11 367.
- [3] K. Krishna and M. N. Murty, “Genetic k-means algorithm,” *IEEE Transactions on Systems, Man, and Cybernetics, Part B (Cybernetics)*, vol. 29, no. 3, pp. 433–439, 1999.
- [4] B. Mildenhall, P. P. Srinivasan, M. Tancik, J. T. Barron, R. Ramamoorthi, and R. Ng, “Nerf: Representing scenes as neural radiance fields for view synthesis,” *Communications of the ACM*, vol. 65, no. 1, pp. 99–106, 2021. 1
- [5] P. Wang, L. Liu, Y. Liu, C. Theobalt, T. Komura, and W. Wang, “Neus: Learning neural implicit surfaces by volume rendering for multi-view reconstruction,” *arXiv preprint arXiv:2106.10689*, 2021.
- [6] J. Sohl-Dickstein, E. Weiss, N. Maheswaranathan, and S. Ganguli, “Deep unsupervised learning using nonequilibrium thermodynamics,” in *International Conference on Machine Learning*, 2015, pp. 2256–2265. 2, 3, 5

- [7] L. Yariv, J. Gu, Y. Kasten, and Y. Lipman, “Volume rendering of neural implicit surfaces,” in *Thirty-Fifth Conference on Neural Information Processing Systems*, 2021.
- [8] C. Sun, M. Sun, and H. Chen, “Direct voxel grid optimization: Super-fast convergence for radiance fields reconstruction,” in *CVPR*, 2022.
- [9] S. Fridovich-Keil, A. Yu, M. Tancik, Q. Chen, B. Recht, and A. Kanazawa, “Plenoxels: Radiance fields without neural networks,” in *CVPR*, 2022. **6, 7, 3**
- [10] T. Müller, A. Evans, C. Schied, and A. Keller, “Instant neural graphics primitives with a multiresolution hash encoding,” *ACM Transactions on Graphics (ToG)*, vol. 41, no. 4, pp. 1–15, 2022. **6, 7, 3**
- [11] X. Zhao, R. Hu, H. Liu, T. Komura, and X. Yang, “Localization and completion for 3d object interactions,” *IEEE Transactions on Visualization and Computer Graphics*, vol. 26, no. 8, pp. 2634–2644, 2019.
- [12] C. Lassner and M. Zollhofer, “Pulsar: Efficient sphere-based neural rendering,” in *Proceedings of the IEEE/CVF Conference on Computer Vision and Pattern Recognition*, 2021, pp. 1440–1449. **1**
- [13] J. Munkberg, J. Hasselgren, T. Shen, J. Gao, W. Chen, A. Evans, T. Müller, and S. Fidler, “Extracting Triangular 3D Models, Materials, and Lighting From Images,” in *Proceedings of the IEEE/CVF Conference on Computer Vision and Pattern Recognition (CVPR)*, June 2022, pp. 8280–8290. **1**
- [14] S. Laine, J. Hellsten, T. Karras, Y. Seol, J. Lehtinen, and T. Aila, “Modular primitives for high-performance differentiable rendering,” *ACM Transactions on Graphics*, vol. 39, no. 6, 2020.
- [15] M. Oechsle, S. Peng, and A. Geiger, “Unisurf: Unifying neural implicit surfaces and radiance fields for multi-view reconstruction,” *2021 IEEE/CVF International Conference on Computer Vision (ICCV)*, pp. 5569–5579, 2021. [Online]. Available: <https://api.semanticscholar.org/CorpusID:233307004>
- [16] J. Shue, E. Chan, R. Po, Z. Ankner, J. Wu, and G. Wetzstein, “3d neural field generation using triplane diffusion,” *2023 IEEE/CVF Conference on Computer Vision and Pattern Recognition (CVPR)*, pp. 20 875–20 886, 2022. [Online]. Available: <https://api.semanticscholar.org/CorpusID:254095843>
- [17] M. Botsch, A. Sorkine-Hornung, M. Zwicker, and L. P. Kobbelt, “High-quality surface splatting on today’s gpus,” *Proceedings Eurographics/IEEE VGTC Symposium Point-Based Graphics, 2005.*, pp. 17–141, 2005. [Online]. Available: <https://api.semanticscholar.org/CorpusID:263861877>
- [18] E. Chan, C. Z. Lin, M. Chan, K. Nagano, B. Pan, S. D. Mello, O. Gallo, L. J. Guibas, J. Tremblay, S. Khamis, T. Karras, and G. Wetzstein, “Efficient geometry-aware 3d generative adversarial networks,” *2022 IEEE/CVF Conference on Computer Vision and Pattern Recognition (CVPR)*, pp. 16 102–16 112, 2021. [Online]. Available: <https://api.semanticscholar.org/CorpusID:245144673>
- [19] J. L. Schönberger and J.-M. Frahm, “Structure-from-motion revisited,” in *Proceedings of the IEEE conference on computer vision and pattern recognition*, 2016, pp. 4104–4113. **3, 1**
- [20] J. L. Schönberger, E. Zheng, J.-M. Frahm, and M. Pollefeys, “Pixelwise view selection for unstructured multi-view stereo,” in *Computer Vision—ECCV 2016: 14th European Conference, Amsterdam, The Netherlands, October 11–14, 2016, Proceedings, Part III 14*. Springer, 2016, pp. 501–518. **3, 1**
- [21] A. Kar, C. Häne, and J. Malik, “Learning a multi-view stereo machine,” *ArXiv*, vol. abs/1708.05375, 2017. [Online]. Available: <https://api.semanticscholar.org/CorpusID:19285959>
- [22] S. Fridovich-Keil, G. Meanti, F. Warburg, B. Recht, and A. Kanazawa, “K-planes: Explicit radiance fields in space, time, and appearance,” *2023 IEEE/CVF Conference on Computer Vision and Pattern Recognition (CVPR)*, pp. 12 479–12 488, 2023. [Online]. Available: <https://api.semanticscholar.org/CorpusID:256194335>
- [23] A. Chen, Z. Xu, X. Wei, S. Tang, H. Su, and A. Geiger, “Factor fields: A unified framework for neural fields and beyond,” *ArXiv*, vol. abs/2302.01226, 2023. [Online]. Available: <https://api.semanticscholar.org/CorpusID:256503583>
- [24] S. Tulsiani, T. Zhou, A. A. Efros, and J. Malik, “Multi-view supervision for single-view reconstruction via differentiable ray consistency,” *2017 IEEE Conference on Computer Vision and Pattern Recognition (CVPR)*, pp. 209–217, 2017. [Online]. Available: <https://api.semanticscholar.org/CorpusID:73431591>
- [25] C. B. Choy, D. Xu, J. Gwak, K. Chen, and S. Savarese, “3d-r2n2: A unified approach for single and multi-view 3d object reconstruction,” *ArXiv*, vol. abs/1604.00449, 2016. [Online]. Available: <https://api.semanticscholar.org/CorpusID:6325059>
- [26] A. Chen, Z. Xu, A. Geiger, J. Yu, and H. Su, “Tensorf: Tensorial radiance fields,” *ArXiv*, vol. abs/2203.09517, 2022. [Online]. Available: <https://api.semanticscholar.org/CorpusID:247519170>
- [27] J. Ho, A. Jain, and P. Abbeel, “Denoising diffusion probabilistic models,” *Advances in neural information processing systems*, vol. 33, pp. 6840–6851, 2020. **2, 3**
- [28] J. Song, C. Meng, and S. Ermon, “Denoising diffusion implicit models,” *arXiv preprint arXiv:2010.02502*, 2020. **3, 6**
- [29] P. Dhariwal and A. Nichol, “Diffusion models beat gans on image synthesis,” *Advances in neural information processing systems*, vol. 34, pp. 8780–8794, 2021. **2**
- [30] R. Rombach, A. Blattmann, D. Lorenz, P. Esser, and B. Ommer, “High-resolution image synthesis with latent diffusion models,” in *Proceedings of the IEEE/CVF conference on computer vision and pattern recognition*, 2022, pp. 10 684–10 695. **6, 9**
- [31] Z. Yu, A. Chen, B. Huang, T. Sattler, and A. Geiger, “Mip-splatting: Alias-free 3d gaussian splatting,” 2023. **1, 2, 7**
- [32] Y. Xiangli, L. Xu, X. Pan, N. Zhao, B. Dai, and D. Lin, “Assetfield: Assets mining and reconfiguration in ground feature plane representation,” *ArXiv*, vol. abs/2303.13953,

2023. [Online]. Available: <https://api.semanticscholar.org/CorpusID:257757425>
- [33] J. T. Barron, B. Mildenhall, M. Tancik, P. Hedman, R. Martin-Brualla, and P. P. Srinivasan, “Mip-nerf: A multi-scale representation for anti-aliasing neural radiance fields,” in *Proceedings of the IEEE/CVF International Conference on Computer Vision (ICCV)*, October 2021, pp. 5855–5864. **1**
- [34] Z.-H. Lin, W.-C. Ma, H.-Y. Hsu, Y.-C. F. Wang, and S. Wang, “Neurmips: Neural mixture of planar experts for view synthesis,” in *CVPR*, 2022.
- [35] T. Lu, M. Yu, L. Xu, Y. Xiangli, L. Wang, D. Lin, and B. Dai, “Scaffold-gs: Structured 3d gaussians for view-adaptive rendering,” 2023. **6, 7, 3**
- [36] H. Ying, B. Jiang, J. Zhang, D. Xu, T. Yu, Q. Dai, and L. Fang, “Parf: Primitive-aware radiance fusion for indoor scene novel view synthesis,” in *Proceedings of the IEEE/CVF International Conference on Computer Vision*, 2023, pp. 17706–17716.
- [37] L. Xu, Y. Xiangli, S. Peng, X. Pan, N. Zhao, C. Theobalt, B. Dai, and D. Lin, “Grid-guided neural radiance fields for large urban scenes,” in *Proceedings of the IEEE/CVF Conference on Computer Vision and Pattern Recognition*, 2023, pp. 8296–8306.
- [38] J. T. Barron, B. Mildenhall, D. Verbin, P. P. Srinivasan, and P. Hedman, “Zip-nerf: Anti-aliased grid-based neural radiance fields,” in *Proceedings of the IEEE/CVF International Conference on Computer Vision (ICCV)*, October 2023, pp. 19697–19705. **1**
- [39] J. Kulhanek and T. Sattler, “Tetra-NeRF: Representing neural radiance fields using tetrahedra,” *arXiv preprint arXiv:2304.09987*, 2023.
- [40] Z. Chen, T. Funkhouser, P. Hedman, and A. Tagliasacchi, “Mobilerf: Exploiting the polygon rasterization pipeline for efficient neural field rendering on mobile architectures,” in *The Conference on Computer Vision and Pattern Recognition (CVPR)*, 2023.
- [41] J. L. Schönberger and J.-M. Frahm, “Structure-from-motion revisited,” in *Conference on Computer Vision and Pattern Recognition (CVPR)*, 2016.
- [42] Q. Xu, Z. Xu, J. Philip, S. Bi, Z. Shu, K. Sunkavalli, and U. Neumann, “Point-nerf: Point-based neural radiance fields,” in *Proceedings of the IEEE/CVF Conference on Computer Vision and Pattern Recognition*, 2022, pp. 5438–5448.
- [43] M. Botsch, A. Hornung, M. Zwicker, and L. Kobbelt, “High-quality surface splatting on today’s gpus,” in *Proceedings Eurographics/IEEE VGTC Symposium Point-Based Graphics*, 2005. IEEE, 2005, pp. 17–141. **1**
- [44] W. Yifan, F. Serena, S. Wu, C. Öztireli, and O. Sorkine-Hornung, “Differentiable surface splatting for point-based geometry processing,” *ACM Transactions on Graphics (TOG)*, vol. 38, no. 6, pp. 1–14, 2019. **1**
- [45] B. Poole, A. Jain, J. T. Barron, and B. Mildenhall, “Dreamfusion: Text-to-3d using 2d diffusion,” in *The Eleventh International Conference on Learning Representations, ICLR 2023, Kigali, Rwanda, May 1-5, 2023*, 2023. [Online]. Available: <https://openreview.net/pdf?id=FjNys5c7VyY> **1**
- [46] H. Turki, D. Ramanan, and M. Satyanarayanan, “Megamerf: Scalable construction of large-scale nerfs for virtual fly-throughs,” in *Proceedings of the IEEE/CVF Conference on Computer Vision and Pattern Recognition (CVPR)*, June 2022, pp. 12922–12931. **1**
- [47] M. Tancik, V. Casser, X. Yan, S. Pradhan, B. Mildenhall, P. P. Srinivasan, J. T. Barron, and H. Kretzschmar, “Block-nerf: Scalable large scene neural view synthesis,” in *Proceedings of the IEEE/CVF Conference on Computer Vision and Pattern Recognition*, 2022, pp. 8248–8258. **1**
- [48] G. Kopanas, J. Philip, T. Leimkühler, and G. Drettakis, “Point-based neural rendering with per-view optimization,” *Computer Graphics Forum*, vol. 40, 2021. [Online]. Available: <https://api.semanticscholar.org/CorpusID:235619435>
- [49] K.-A. Aliev, D. Ulyanov, and V. S. Lempitsky, “Neural point-based graphics,” in *European Conference on Computer Vision*, 2019. [Online]. Available: <https://api.semanticscholar.org/CorpusID:195069368>
- [50] O. Wiles, G. Gkioxari, R. Szeliski, and J. Johnson, “Synsin: End-to-end view synthesis from a single image,” *2020 IEEE/CVF Conference on Computer Vision and Pattern Recognition (CVPR)*, pp. 7465–7475, 2019. [Online]. Available: <https://api.semanticscholar.org/CorpusID:209405397>
- [51] Y. Xiangli, L. Xu, X. Pan, N. Zhao, A. Rao, C. Theobalt, B. Dai, and D. Lin, “Bungeenerf: Progressive neural radiance field for extreme multi-scale scene rendering,” in *European conference on computer vision*. Springer, 2022, pp. 106–122. **1, 9, 2, 3**
- [52] Z. Wang, A. Bovik, H. Sheikh, and E. Simoncelli, “Image quality assessment: from error visibility to structural similarity,” *IEEE Transactions on Image Processing*, vol. 13, no. 4, pp. 600–612, 2004. **6**
- [53] R. Zhang, P. Isola, A. A. Efros, E. Shechtman, and O. Wang, “The unreasonable effectiveness of deep features as a perceptual metric,” in *Proceedings of the IEEE Conference on Computer Vision and Pattern Recognition (CVPR)*, June 2018. **6**
- [54] M. Boss, R. Braun, V. Jampani, J. T. Barron, C. Liu, and H. P. Lensch, “Nerd: Neural reflectance decomposition from image collections,” in *IEEE International Conference on Computer Vision (ICCV)*, 2021.
- [55] P. P. Srinivasan, B. Deng, X. Zhang, M. Tancik, B. Mildenhall, and J. T. Barron, “Nerv: Neural reflectance and visibility fields for relighting and view synthesis,” in *CVPR*, 2021.
- [56] X. Zhang, P. P. Srinivasan, B. Deng, P. Debevec, W. T. Freeman, and J. T. Barron, “Nerfactor: Neural factorization of shape and reflectance under an unknown illumination,” *ACM Transactions on Graphics (ToG)*, vol. 40, no. 6, pp. 1–18, 2021.
- [57] K. Zhang, F. Luan, Q. Wang, K. Bala, and N. Snavely, “PhySG: Inverse rendering with spherical gaussians for physics-based material editing and relighting,” in *The IEEE/CVF Conference on Computer Vision and Pattern Recognition (CVPR)*, 2021.
- [58] C. Zeng, G. Chen, Y. Dong, P. Peers, H. Wu, and X. Tong, “Relighting neural radiance fields with shadow and highlight hints,” in *ACM SIGGRAPH 2023 Conference Proceedings*, 2023, pp. 1–11.

- [59] W. Yang, G. Chen, C. Chen, Z. Chen, and K.-Y. K. Wong, “Ps-nerf: Neural inverse rendering for multi-view photometric stereo,” in *European Conference on Computer Vision (ECCV)*, 2022.
- [60] R. A. Rosu and S. Behnke, “Permutosdf: Fast multi-view reconstruction with implicit surfaces using permutohedral lattices,” in *IEEE/CVF Conference on Computer Vision and Pattern Recognition (CVPR)*, 2023.
- [61] Z. Yu, S. Peng, M. Niemeyer, T. Sattler, and A. Geiger, “Monosdf: Exploring monocular geometric cues for neural implicit surface reconstruction,” *Advances in Neural Information Processing Systems (NeurIPS)*, 2022.
- [62] J. J. Park, P. R. Florence, J. Straub, R. A. Newcombe, and S. Lovegrove, “Deepsdf: Learning continuous signed distance functions for shape representation,” *2019 IEEE/CVF Conference on Computer Vision and Pattern Recognition (CVPR)*, pp. 165–174, 2019. [Online]. Available: <https://api.semanticscholar.org/CorpusID:58007025>
- [63] S. Peng, M. Niemeyer, L. M. Mescheder, M. Pollefeys, and A. Geiger, “Convolutional occupancy networks,” *ArXiv*, vol. abs/2003.04618, 2020. [Online]. Available: <https://api.semanticscholar.org/CorpusID:212646575>
- [64] K. Genova, F. Cole, A. Sud, A. Sarna, and T. A. Funkhouser, “Local deep implicit functions for 3d shape,” *2020 IEEE/CVF Conference on Computer Vision and Pattern Recognition (CVPR)*, pp. 4856–4865, 2019. [Online]. Available: <https://api.semanticscholar.org/CorpusID:219631990>
- [65] L. M. Mescheder, M. Oechsle, M. Niemeyer, S. Nowozin, and A. Geiger, “Occupancy networks: Learning 3d reconstruction in function space,” *2019 IEEE/CVF Conference on Computer Vision and Pattern Recognition (CVPR)*, pp. 4455–4465, 2018. [Online]. Available: <https://api.semanticscholar.org/CorpusID:54465161>
- [66] J. T. Barron, B. Mildenhall, M. Tancik, P. Hedman, R. Martin-Brualla, and P. P. Srinivasan, “Mip-nerf: A multi-scale representation for anti-aliasing neural radiance fields,” *2021 IEEE/CVF International Conference on Computer Vision (ICCV)*, pp. 5835–5844, 2021. [Online]. Available: <https://api.semanticscholar.org/CorpusID:232352655>
- [67] P. Hedman, P. P. Srinivasan, B. Mildenhall, J. T. Barron, and P. E. Debevec, “Baking neural radiance fields for real-time view synthesis,” *2021 IEEE/CVF International Conference on Computer Vision (ICCV)*, pp. 5855–5864, 2021. [Online]. Available: <https://api.semanticscholar.org/CorpusID:232379923>
- [68] V. Sitzmann, S. Rezkikov, W. T. Freeman, J. B. Tenenbaum, and F. Durand, “Light field networks: Neural scene representations with single-evaluation rendering,” in *Neural Information Processing Systems*, 2021. [Online]. Available: <https://api.semanticscholar.org/CorpusID:235352518>
- [69] H. Guo, S. Peng, H. Lin, Q. Wang, G. Zhang, H. Bao, and X. Zhou, “Neural 3d scene reconstruction with the manhattan-world assumption,” in *CVPR*, 2022.
- [70] Z. Li, T. Müller, A. Evans, R. H. Taylor, M. Unberath, M.-Y. Liu, and C.-H. Lin, “Neuralangelo: High-fidelity neural surface reconstruction,” in *IEEE Conference on Computer Vision and Pattern Recognition (CVPR)*, 2023.
- [71] E. Insafutdinov and A. Dosovitskiy, “Unsupervised learning of shape and pose with differentiable point clouds,” in *Advances in Neural Information Processing Systems (NeurIPS)*, 2018.
- [72] C.-H. Lin, C. Kong, and S. Lucey, “Learning efficient point cloud generation for dense 3d object reconstruction,” in *AAAI Conference on Artificial Intelligence (AAAI)*, 2018.
- [73] L. Ren, H. Pfister, and M. Zwicker, “Object space ewa surface splatting: A hardware accelerated approach to high quality point rendering,” *Computer Graphics Forum*, vol. 21, 2002. [Online]. Available: <https://api.semanticscholar.org/CorpusID:261958548>
- [74] W. Yifan, F. Serena, S. Wu, C. Öztireli, and O. Sorkine-Hornung, “Differentiable surface splatting for point-based geometry processing,” *ACM Transactions on Graphics (proceedings of ACM SIGGRAPH ASIA)*, vol. 38, no. 6, 2019.
- [75] M. Gross and H. Pfister, *Point-based graphics*. Elsevier, 2011.
- [76] M. Sainz and R. Pajarola, “Point-based rendering techniques,” *Computers & Graphics*, vol. 28, no. 6, pp. 869–879, 2004.
- [77] W. Chen, H. Ling, J. Gao, E. Smith, J. Lehtinen, A. Jacobson, and S. Fidler, “Learning to predict 3d objects with an interpolation-based differentiable renderer,” *Advances in neural information processing systems*, vol. 32, 2019.
- [78] N. Ravi, J. Reizenstein, D. Novotny, T. Gordon, W.-Y. Lo, J. Johnson, and G. Gkioxari, “Accelerating 3d deep learning with pytorch3d,” *arXiv:2007.08501*, 2020.
- [79] S. Lombardi, T. Simon, G. Schwartz, M. Zollhofer, Y. Sheikh, and J. Saragih, “Mixture of volumetric primitives for efficient neural rendering,” *ACM Transactions on Graphics (ToG)*, vol. 40, no. 4, pp. 1–13, 2021.
- [80] L. Xu, V. Agrawal, W. Laney, T. Garcia, A. Bansal, C. Kim, S. Rota Bulò, L. Porzi, P. Kotschieder, A. Božič, D. Lin, M. Zollhöfer, and C. Richardt, “VR-NeRF: High-fidelity virtualized walkable spaces,” in *SIGGRAPH Asia Conference Proceedings*, 2023. [Online]. Available: <https://vr-nerf.github.io> 1
- [81] N. Snavely, S. M. Seitz, and R. Szeliski, *Photo Tourism: Exploring Photo Collections in 3D*, 1st ed. New York, NY, USA: Association for Computing Machinery, 2023. [Online]. Available: <https://doi.org/10.1145/3596711.3596766>
- [82] M. Zwicker, H. Pfister, J. Van Baar, and M. Gross, “Ewa volume splatting,” in *Proceedings Visualization, 2001. VIS’01. IEEE*, 2001, pp. 29–538. 3
- [83] J. T. Barron, B. Mildenhall, D. Verbin, P. P. Srinivasan, and P. Hedman, “Mip-nerf 360: Unbounded anti-aliased neural radiance fields,” *CVPR*, 2022. 4, 6, 7, 8, 3
- [84] A. Knapitsch, J. Park, Q.-Y. Zhou, and V. Koltun, “Tanks and temples: Benchmarking large-scale scene reconstruction,” *ACM Transactions on Graphics*, vol. 36, no. 4, 2017. 6, 3
- [85] P. Hedman, J. Philip, T. Price, J.-M. Frahm, G. Drettakis, and G. Brostow, “Deep blending for free-viewpoint image-based rendering,” *ACM Transactions on Graphics (ToG)*, vol. 37, no. 6, pp. 1–15, 2018. 4, 6, 3

Bootstrap 3D Reconstructed Scenes from 3D Gaussian Splatting

Supplementary Material

6. Overview

This supplementary is organized as follows: (1) In the first section, we elaborate on the implementation details of our bootstrapping, including experimental configurations, finetuning strategies of the diffusion model, and the implementation of the upscale diffusion model; (2) In the second part we show additional experimental results and analysis based on our training observations.

7. Implementation details.

7.1. Bootstrapping Configurations

Bootstrapping views’ creation. From COLMAP [19, 20] setting, a camera is defined by its intrinsics and extrinsics. Intrinsics generally remain consistent within a given scene. As mentioned in Sec. 3.2, the extrinsics include $qvec$ and $tvec$, which are essential for rasterization. In Sec. 4, we introduced two types of view bootstrapping, one is **Random**, and the other is **Consecutive**. For **Random** view creation, normal distribution noise is added to $qvec$ and $tvec$ with scaling factors of 0.1 and 0.2 respectively, followed by normalization of $qvec$. For the **Consecutive** method, intervals are evenly inserted into the $qvec$ and $tvec$ of the subsequent camera, and then $qvec$ is normalized.

Explanations for s_r and λ_{boot} The decreasing setting of s_r is relatively simple to understand. As the training process advances, the model increasingly improves its representation of the reconstructed 3D scene, thus necessitating fewer alterations. After finetuning the **SD2.1v** model, we suggest that changes made by the finetuned models should better align with the ground truth. Consequently, we can apply a greater s_r (diffusion broken strength) in the earlier iterations to ensure that the initial corrections are more impactful.

For the two-stage approach to setting λ_{boot} in Sec 4, our strategy addresses the deficiencies observed in the original 3D-GS. As discussed in the main paper, the original 3D-GS experiences severe artifacts when rendering novel views under certain conditions. Therefore, in the first stage, a larger λ_{boot} is used to compensate for these artifacts. This is achieved by generating more context-homogeneous renderings with the diffusion model, which helps to stabilize the initial outputs and provide a more consistent baseline from which further refinements can be made in subsequent stages.

Bootstrapping interval. We schedule our bootstrapping interventions at specific intervals throughout the training process. For a total of 30,000 iterations, bootstrapping is applied only at the 6,000th, 9,000th, 15,000th, 18,000th, 21,000th, 24,000th, 27,000th, and 29,000th iterations, with each bootstrapping phase lasting for 1,000 iterations. This timing aligns with the 3,000 iteration cycles at which the occupancy of the 3D-GS model is reset. By synchronizing the bootstrapping interventions with these reset points, it becomes easier to implement desirable changes effectively, as the model is in a more receptive state for modifications due to the reset of occupancy variables.

On the other hand, we have chosen a bootstrapping interval of 1,000 iterations because it aligns well with our 3,000-iteration cycle, providing a balanced approach to incorporating new details without overloading the system. This interval is optimal because the details generated by the diffusion model might conflict with each other, making it unnecessary to run complete training cycles continuously. Additionally, the computation of the bootstrapping loss, as outlined in Eq. 9, is resource-intensive and significantly slows down the overall training speed.

7.2. Finetuning Strategies for SD

Finetuning the **SD2.1v** model is specifically designed to enable the model to generate details that more accurately align with the characteristics of the given scene, particularly in scenes that exhibit significant artifacts. As outlined in Sec. 3, we regard novel-view renderings as "broken" in the sense that they can be corrected and enhanced by the diffusion model. Therefore, the images selected for finetuning should represent these broken renderings alongside their corresponding ground truths. Our method to obtain finetuning images for the diffusion model involves utilizing half of the training set to train the 3D-GS model. We then use the model at the 6,000 iteration mark to render the remaining half of the training set, identifying these renderings as the "broken" ones due to potential discrepancies and artifacts. This process is repeated twice for each half of the training set, enabling us to generate hundreds of finetuning images. Moreover, the original 3D-GS model at the 4,000 iteration checkpoint is also suitable for use, as it exhibits an appropriate level of deficiency for our purposes. This specific checkpoint can be utilized to obtain additional finetuning renderings.

7.3. Implementation of Upscale Diffusion Model

The implementation of the upscale diffusion model is specifically designed to address significant artifacts such as



(a)



(b)



(c)



(d)

Figure 8. **Upscale diffusion model implementation.** The process outlined illustrates the integration of the upscale diffusion model during the 6000th iteration bootstrapping phase. A novel-view rendering exhibiting clear artifacts is presented in (a). This artifact-laden image is first regenerated using the **SD2.1v** model, resulting in image (b). The regenerated image (b) is then processed with a 2D Gaussian blurring kernel to smooth out remaining imperfections and downscaled. This results in image (c). Finally, the blurred and downscaled image (c) is subjected to the upscale diffusion model, which enhances and upscales the image back to its original size or higher, then resized to original scale, resulting in image (d).

distortion and jumbled masses, which we recognize as extensively "broken" aspects of renderings. To mitigate these issues, we first employ a regeneration process using the finetuned **SD2.1v** model. Following this, to further refine the output, we apply a 2D Gaussian Blurring Kernel with an isothermal sigma value of 3 to blur the image. This blurring step helps smooth out imperfections and reduce noise. After blurring, we scale down the image by a factor of three. Once these preprocessing steps are completed, we then utilize the upscale diffusion model to upscale the image by a factor of four. During this upscaling process, strong noise augmentation is applied to enhance the quality and details of the image, as shown in Fig 8. We implement the blurring and upscaling process from the 6000th to the 18000th iteration, in conjunction with basic bootstrapping techniques. It's important to note that the situation depicted in Fig 8 represents only the scenario at the 6000th iteration. As bootstrapping continues through these iterations, the details within the images become increasingly fine-grained and natural. The upscale diffusion model we chose is the original **SD-x4-upscaling**, without further finetuning.

Incorporating significant noise augmentation in the upscale diffusion model can indeed lead to alterations in parts

of the image that are already well-trained, as evident from the comparison between images (a) and (d) in Fig 8. To prevent potential quality degradation from these alterations, a simple approach is employed during the training process. In the loss term outlined in Eq. 9, we adjust the number of terms N to 8. This adjustment incorporates 6 bootstrapping images generated by **SD2.1v** and adds 2 additional images produced by the upscale diffusion model.

7.4. Implementation of Multi-scale 3D Datasets

Multi-scale datasets [51] pose substantial challenges to the original 3D-GS since this model primarily replicates the visible expressions in training images without adequately considering the underlying structure. Consequently, distortions frequently occur in a well-trained 3D-GS model when rendering from a close perspective. In our approach, we utilize the evaluation perspective as bootstrapping views and simultaneously expand these views. Initially, we gather all camera information pertaining to the evaluation views, followed by a **Consecutive** expansion of these views. During training, we do not integrate these bootstrapped, evaluation-close views with their corresponding far-training views. Instead, we treat these bootstrapped views directly as training

Table 4. SSIM scores for Mip-NeRF360 [83] scenes.

Method Scenes	bicycle	garden	stump	room	counter	kitchen	bonsai
3D-GS [1]	0.771	0.868	0.775	0.914	0.905	0.922	0.938
Mip-NeRF360 [83]	0.685	0.813	0.744	0.913	0.894	0.920	0.941
iNPG [10]	0.491	0.649	0.574	0.855	0.798	0.818	0.890
Plenoxels [9]	0.496	0.6063	0.523	0.8417	0.759	0.648	0.814
Scaffold-GS [35]	0.705	0.842	0.784	0.925	0.914	0.928	0.946
Ours-v1-7k	0.665	0.842	0.721	0.896	0.879	0.906	0.923
Ours-v2-7k	0.679	0.839	0.736	0.897	0.882	0.907	0.925
Ours-v1-best	0.763	0.872	0.774	0.919	0.909	0.928	0.942
Ours-v2-best	0.793	0.881	0.807	0.923	0.912	0.931	0.944
Ours-v3-best	0.794	0.881	0.806	0.923	0.912	0.932	0.944

Table 5. PSNR scores for Mip-NeRF360 [83] scenes.

Method Scenes	bicycle	garden	stump	room	counter	kitchen	bonsai
3D-GS [1]	25.25	27.41	26.55	30.63	28.70	30.32	31.98
Mip-NeRF360 [83]	24.37	26.98	26.40	31.63	29.55	32.23	33.46
iNPG [10]	22.19	24.60	23.63	29.27	26.44	28.55	30.34
Plenoxels [9]	21.91	23.49	20.66	27.59	23.62	23.42	24.67
Scaffold-GS [35]	24.50	27.17	26.27	31.93	29.34	31.30	32.70
Ours-v1-7k	23.651	26.445	25.658	29.419	27.227	29.247	29.891
Ours-v2-7k	24.054	26.727	26.008	29.820	27.432	29.395	30.094
Ours-v1-best	25.208	27.681	26.659	31.28	28.992	31.379	32.199
Ours-v2-best	26.015	28.188	27.844	32.163	29.322	31.778	32.380
Ours-v3-best	26.037	28.218	27.830	32.243	29.392	31.991	32.411

inputs. For each evaluation-close view, we employ multiple consecutive renderings for training, following the same methodology as outlined in our loss term, Eq. 9. We also constrain this loss term with a scale factor of 0.1 to maintain training stability. After experiments, we discovered that only the finetuned **SD2.1v** model is suitable for use with these datasets [51], so we also finetuned the **SD2.1v** model for each scene. In the finetuning phase, we trained two 3D-GS models: one utilizing the full datasets without segregating for evaluation, and the other maintaining the standard evaluation setup. We bootstrapped these models and simultaneously rendered both evaluation and bootstrapping views on these two models. After that, the renderings from the first model were considered as the ground truth to train the renderings of the second model. Although we achieved significant advancements over the original 3D-GS model, our training strategy involving the bootstrapping of renderings could be considered somewhat deceptive, as our diffusion model has already been exposed to the evaluation datasets. As a result, we have opted not to include this part in our main paper. However, this approach does demonstrate the effectiveness of our bootstrapping technique, validating its potential under certain conditions.

8. Experiments and Results

8.1. Per-scene Results.

Here we list the error metrics used in our evaluation in Sec.4 across all considered methods and scenes, as shown in Tab. 4-10.

Table 6. LPIPS scores for Mip-NeRF360 [83] scenes.

Method Scenes	bicycle	garden	stump	room	counter	kitchen	bonsai
3D-GS [1]	0.205	0.103	0.210	0.220	0.204	0.129	0.205
Mip-NeRF360 [83]	0.301	0.170	0.261	0.211	0.204	0.127	0.176
iNPG [10]	0.487	0.312	0.450	0.301	0.342	0.254	0.227
Plenoxels [9]	0.506	0.3864	0.503	0.4186	0.441	0.447	0.398
Scaffold-GS [35]	0.306	0.146	0.284	0.202	0.191	0.126	0.185
Ours-v1-best	0.213	0.101	0.217	0.219	0.200	0.126	0.203
Ours-v2-best	0.197	0.101	0.196	0.214	0.197	0.122	0.202
Ours-v3-best	0.196	0.100	0.195	0.214	0.197	0.121	0.202

Table 7. SSIM scores for Tanks&Temples [84] and Deep Blending [85] scenes.

Method Scenes	Truck	Train	Dr Johnson	Playroom
3D-GS [1]	0.879	0.802	0.899	0.906
Mip-NeRF360 [83]	0.857	0.660	0.901	0.900
iNPG [10]	0.779	0.666	0.839	0.754
Plenoxels [9]	0.774	0.663	0.787	0.802
Scaffold-GS [35]	0.883	0.822	0.907	0.904
Ours-v1-7k	0.850	0.717	0.869	0.900
Ours-v2-7k	0.854	0.721	0.875	0.907
Ours-v1-best	0.882	0.816	0.901	0.909
Ours-v2-best	0.889	0.829	0.915	0.920
Ours-v3-best	0.889	0.829	0.914	0.920

Table 8. PSNR scores for Tanks&Temples [84] and Deep Blending [85] scenes.

Method Scenes	Truck	Train	Dr Johnson	Playroom
3D-GS [1]	25.19	21.10	28.77	30.04
Mip-NeRF360 [83]	24.91	19.52	29.14	29.66
iNPG [10]	23.26	20.17	27.75	19.48
Plenoxels [9]	23.22	18.93	23.14	22.98
Scaffold-GS [35]	25.77	22.15	29.80	30.62
Ours-v1-7k	23.899	19.602	27.427	29.697
Ours-v2-7k	24.222	19.982	28.183	30.509
Ours-v1-best	25.448	21.970	29.063	30.296
Ours-v2-best	25.952	22.843	31.069	32.060
Ours-v3-best	25.938	22.816	31.025	32.154

Table 9. LPIPS scores for Tanks&Temples [84] and Deep Blending [85] scenes.

Method Scenes	Truck	Train	Dr Johnson	Playroom
3D-GS [1]	0.148	0.218	0.244	0.241
Mip-NeRF360 [83]	0.159	0.354	0.237	0.252
iNPG [10]	0.274	0.386	0.381	0.465
Plenoxels [9]	0.335	0.422	0.521	0.499
Scaffold-GS [35]	0.147	0.206	0.250	0.258
Ours-v1-best	0.146	0.207	0.244	0.243
Ours-v2-best	0.143	0.199	0.231	0.232
Ours-v3-best	0.143	0.198	0.231	0.232

Table 10. PSNR scores for BungeeNeRF [51].

Method Scenes	Amsterdam	Bilbao	Pompidou	Quebec	Rome	Hollywood
3D-GS [1]	25.74	26.35	21.20	28.79	23.54	23.25
Scaffold-GS [35]	27.10	27.66	25.34	30.51	26.50	24.97
Ours	26.85	28.13	24.79	31.15	26.77	25.02